RSC Advances

PAPER

View Article Online
View Journal | View Issue

Cite this: *RSC Adv.*, 2024, **14**, 25830

Cu-P@silica-CNT-based catalyst for effective electrolytic water splitting in an alkaline medium with hydrazine assistance†

Nezar H. Khdary, *[a] Asmaa R. M. El-Gohary,[b] Ahmed Galal, [b] Ahmed M. Alhassan[a] and Sami D. Alzahrain[a]

In this study, we prepared a potential catalyst as an electrode modifier for electrolytic water splitting. In the preparation step, the amine was decorated with copper–phosphorus. It was immobilized over the silica surface, and the surface was engineered using *N*-(3-(trimethoxysilyl) propyl)ethylenediamine for the synthesis of the catalysts (AS). The morphological and structural aspects of the catalyst (AFS-Cu-P) were determined using FE-SEM/EDAX, FTIR, elemental analysis, BET, TGA, and XPS. The catalyst's efficacy for the oxygen evolution reaction (OER) was assessed in an alkaline medium with and without hydrazine. The hydrazine oxidation reaction enhanced the sluggish OER and facilitated water splitting. Detailed electrochemical measurements confirmed an increase in the kinetics of the process and a reduction in the activation energy needed to complete the process. The Tafel slopes, charge transfer coefficients, exchange-specific current densities, apparent rate constants, and diffusion coefficients are provided along with their respective values. The results showed that the presence of Cu and CNT is crucial in the conversion process.

Received 30th May 2024
Accepted 18th July 2024

DOI: 10.1039/d4ra03998j

rsc.li/rsc-advances

1 Introduction

The growing demand for energy is reflected in the exhaustive fossil fuel usage that consequently increases CO_2 generation and impacts climate change. Therefore, the demand for CO_2-emission reduction and a "green" fuel alternative has grown in the last decade.[1] Hydrogen production has been targeted for use as a "clean" fuel, namely in hydrogen fuel cells, and several routes have been suggested for its green production and CO_2 reduction.[2] Among the green pathways for hydrogen generation is water electrolysis, which has been more recently described as water splitting.[3] Despite the progress in the design of anion and proton exchange membranes, developing electrocatalysts for water splitting that tolerate long-term usage and high temperature while providing low overpotential values for the electrochemical process, and their possible employment in harsh electrolytic conditions, remains a challenge.[4]

Different approaches have been suggested to boost the charge transfer reaction, such as the hydrogen evolution reaction (HER) and oxygen evolution reaction for water electrolysis;[5–7] as well as the hydrogen oxidation reaction (HOR) and oxygen reduction reaction (ORR) for fuel cell applications.[8–12] Among the most commonly used electrocatalysts are Ni-based materials;[13–15] advanced approaches have also been proposed by combining a bimetallic Ni–Fe catalyst with an organic framework on nickel foam.[16] Iron-based catalysts have been successfully employed for electrolytic water splitting,[17–19] and other catalysts such as perovskites with different structures have also been used.[20–22] Recently, extensive research has been directed toward photoelectrochemical approaches, either using photovoltaics to generate electricity for the electrolysis process or by designing photoelectrochemical catalysts, including semiconductors and their junctions.[22–29]

Copper is among the promising metals used as a component in several catalytic forms for electrolytic water splitting, such as nanoparticles, heterojunction semiconductors, binary metals, hybrids, multielement, and photoelectrochemical catalysts.[30–40] Copper is among the earth-abundant metals; therefore, its use as an electrocatalyst for water splitting will not present scarcity issues for upscaling production. In addition to its low cost and ease of processing compared to other currently used catalysts, copper possesses unique properties including high electrical conductivity, multiple valence states, high ductility, and thermal conductance. The insertion of copper with other components into the structure of the catalysts used for water splitting results in the adjustment of the electronic configuration of the material and lowers the activation energy required for the electrolysis process. A key condition for the effectiveness of electrocatalysts in the water-splitting process is the homogeneous distribution of the catalysts over the substrate.[41,42] The

[a]*King Abdulaziz City for Science and Technology, Riyadh 11442, Kingdom of Saudi Arabia. E-mail: nhkdary@kacst.edu.sa*

[b]*Cairo University, Faculty of Science, Chemistry Department, Giza, 12613, Egypt*

† Electronic supplementary information (ESI) available. See DOI: https://doi.org/10.1039/d4ra03998j

water-splitting reaction is known to be controlled by the oxidation half-reaction, the OER, which is devoid of both energetic and kinetic energy. Overcoming this step is the key to the successful production of oxygen and hydrogen gasses *via* electrolysis.[43]

Hydrazine (HH) is considered among the most favorable compounds that promote the water-splitting process through its electrooxidation. The charge transfer for the water oxidation process is kinetically facilitated by the lower activation energy of HH oxidation.[44–46] The hydrazine electrochemical oxidation (HEO) has been shown to assist the HER when using several catalytic surfaces.[47,48] In addition, the HEO assists the OER (E = 1.23 V *vs.* RHE) as a half-reaction, as indicated earlier.[49]

The reaction for the HEO can be written as:[46,50]

$$N_2H_4 + 4OH^- \rightarrow N_2 + 4H_2O + 4e^- \quad (E = -0.33 \text{ V } \textit{vs.} \text{ RHE}) \quad (1)$$

The anodic half-reaction of the OER, impeded by its slow kinetics and the energy barrier that must be overcome, prevents water splitting *via* electrolysis.

Therefore, several catalysts have been devised to facilitate the process, including individual metals such as nickel, cobalt, iron, *etc.*, or binary metals.[44,45,48,51–56] These catalysts and others may also be used in conjunction with an anodic conversion of small molecules such as urea, hydrazine, and alcohol with a relatively lower energy barrier. With the extensive investigation of water splitting and the need to develop catalysts that are easily prepared based on non-noble metals with high efficiency for conversion and energy-saving procedures for their preparation, we are presenting this work.[13,57–59] To accomplish this and overcome the challenges, numerous catalysts have been developed; however, these catalysts have certain disadvantages, such as the length of the treatment process, the cost of materials, and the sustainability of the catalyst's use. In this method, silica was used as the core, and its surface was modified with a diamine compound; the amine was then decorated with copper–phosphorus. This catalyst exhibited good productivity with outstanding stability during the experiments. To achieve this, a new Cu-containing catalyst supported over silica-based materials was prepared. Surface modification for the synthesis of the catalysts allowed control over the prepared materials' composition and characteristics. Copper-based catalysts, namely oxides and hydroxides, are good candidates for the oxygen evolution reaction (OER).[60,61] These catalysts face challenges when employed for the hydrogen evolution reaction (HER) due to their low ionic conductivity. It was suggested that when the Cu-catalyst is applied over a conducting surface such as graphene or carbon nanotubes, it results in lowering the overpotential needed for the process.[62] Copper is considered a good candidate as an electrocatalyst since it belongs to the first row of transition elements. Copper is characterized with several advantages, such as being among the abundant elements and having two different redox states and high conductivity.[63] Previous studies have shown that copper-based heterogeneous catalysis based on Cu(0)/Cu(I) conversion can be used for the HER, while Cu(III) because of its high reduction potential, provides active sites for the OER.[64]

This work considered the systematic evaluation of the performance of the catalyst to report its relative efficiency for the OER reaction. Hydrazine was used as a promoter for the electrolysis process and multi-walled carbon nanotubes were employed as a support that allowed homogeneous surface distribution for the catalyst. When using a relatively small amount of the catalyst (as low as 5.0×10^{-6} g), the overpotential for the OER was 0.2 V *vs.* NHE for a specific current density of 10 mA g^{-1} cm^{-2} in the presence of 0.33 M hydrazine/1.0 M KOH. The values of the apparent diffusion coefficients, rate constant, Tafel slopes, and charge transfer coefficients are reported and compared with the different surfaces used.

2 Experimental

2.1. Chemicals

Silica gel (Ultrapure, with a particle size of 40–60 mm and pore size of 60 Å) was purchased from ACROS Organic (USA). *N*-(3-(trimethoxysilyl)propyl)ethylenediamine, (Acros, USA), toluene, and methanol were obtained from Prolabo, Europe. Copper sulfate ($Cu(SO_4)_5H_2O$) and phosphorus standard solution (1000 μg mL^{-1}) were obtained from (Merck, UK). Potassium hydroxide (anhydrous, ≥99.95%), hydrazine hydrate (RG, N_2H_4 50–60%), and multi-walled carbon nanotubes (CNTs; O.D. = 10–15 nm, I.D. = 2–6 nm, L = 0.1–10 μm, >90% AS) were acquired through Sigma-Aldrich (USA). All compounds were utilized without any additional processing.

2.2. Structural and surface analysis equipment

The samples were characterized using 64 scans of mid-infrared absorption spectra obtained using an FT-IR spectrometer (Vertex 70, Bruker, Germany) at a resolution of 4 cm^{-1}, and the analysis was conducted using ATR Multiple Crystal Dimond. The catalyst spectra were acquired using UV-vis diffuse reflectance spectra with an integrating sphere-equipped PerkinElmer Lambda 950 spectrophotometer with a resolution of 1 nm. An X-ray diffractometer (D8 Advance, Bruker, Germany) with 40 kV, 40 mA, and Cu-Kα X-ray source of 2.2 kW was used to obtain phase characterization. Using a TGA thermal analyzer (STD-Q 600, USA) in a helium environment, the sample weight loss was measured at ambient temperature and temperatures up to 800 °C at a rate of 10 °C min^{-1}. Utilizing a JSM-7800F scanning electron microscope, the microstructure of the generated catalysts was captured, and Oxford Instruments X-Max^N electron dispersive X-ray spectroscopy (EDS) equipment was employed to analyze the elements. Using monochromatic Al Kα radiation ($h\nu$ = 1486.6 eV), X-ray photoelectron spectroscopy (XPS) data were obtained using a JPS-9200 X-ray photoelectron spectrometer.

2.3. Functionalization

The functionalization of silica was performed using a 250 mL round-bottom flask connected with a reflux condenser. First, 150 mL of dry toluene was added to 5.0 g of the silica and kept under stirring, and the reaction environment was kept under nitrogen with stirring. The temperature was increased to 70 °C, and after maintaining the temperature at 70 °C, 3 mL of *N*-[3-

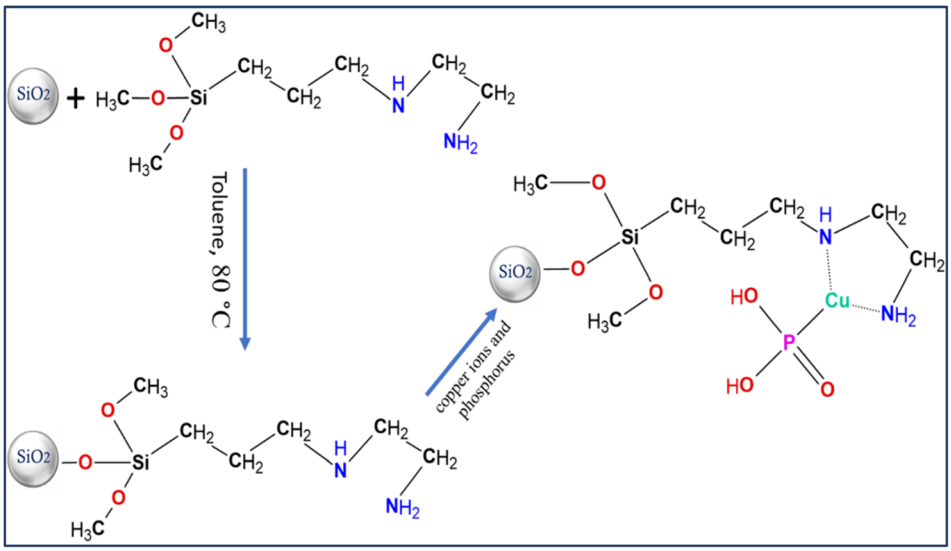

Scheme 1 Schematic of the modification process.

(trimethoxysilyl)propyl]ethylenediamine was slowly dropped to the reaction. The temperature was then raised to 80 °C, and the reaction was continued for 7 h. The reaction was then cooled to ambient temperature. Centrifugation was used to separate the modified silica particles, which were then completely rinsed with toluene and methanol and dried overnight at 50 °C under vacuum.

The assimilation of copper ions and phosphorus into the modified silica was performed by transferring 0.5 g of modified silica into a 10 mL screw-top vial with a cap. Then, 4 mL of 1.0 M $Cu(SO_4)_5H_2O$ and 4 mL of phosphorous solution were incorporated at the same time and shaken for 4 h. The suspension was rinsed, the unreacted material was removed by centrifugation, and the product was rinsed using deionized water five times and ultimately vacuum-dried at 60 °C before characterization (Scheme 1).

2.4. Electrochemical instrumentation and cell

A PGZ301 Voltalab Galvanostat/Potentiostat (Radiometer Analytical, USA) was used to measure voltammetry and chronoamperometry in a three-electrode cell setup: Ag/AgCl (3.0 mol L^{-1} KCl) served as the reference electrode, glassy carbon electrode (GC) (φ: 6.0 mm) served as the working electrode, and Pt wire (l: 10 cm, φ: 2.0 mm) serves as the auxiliary electrode. Electrochemical impedance spectroscopy (EIS) measurements were performed using a metrohm PGSTAT302N potentiostat attached to an FRA32M module. The EIS experiment conditions were as follows: a dc potential equal to the onset potential of OER was applied at each electrode surface, and the frequency was varied from 100 mHz to 100 kHz using an AC amplitude of 10 mV. The data fitting and modeling were obtained using the software provided with the instrument. Linear sweep voltammetry curves were recorded from $E_i = 0.1$ V to $E_f = 0.7$ V at a scan rate of 10 mV s^{-1}. The Tafel experiments were carried out at a scan rate of 1 mV s^{-1}. Chronoamperometry experiments were performed by applying a constant applied potential equivalent to the oxidation potential of hydrazine at a given catalyst surface for 1–2 h.

2.5. Electrode preparation

First, 0.5 mg of solid catalyst and 1.0 mL of DMF were physically mixed to create the catalyst ink, which was subsequently physically mixed with CNTs in various ratios. To make sure that all of the ingredients were distributed evenly, the mixes were sonicated for one hour. The electrode surface was prepared by mechanically polishing the surface using different grades of polishing papers and finally cleaning grease and adsorbed particles from it using different solvents and sonication in distilled water. The electrode was placed in an oven for 10 min at 60 °C to dry. The calculated amount of catalyst on the surface was 5.0×10^{-6} g.

3 Results and discussion

3.1. Surface characteristics

Scheme 1 illustrates the various steps involved in the creation of the solid, in which silica particles combine with the silene agent, which results in the presence of amine groups on the silica surface. In the ultimate phase, the solid compound is produced through the combination of copper–phosphorus ions with the aforementioned amine groups. The optical image provided below (Fig. 1) showcases the distinct colors of amine silica, amine silica bonded with copper ions, and ultimately, the copper–phosphorus-bound amine silica.

3.1.1. Scanning electron microscopy (SEM). The surface images of the as-prepared AFS-Cu(II) and AFS-Cu-P catalysts were identified by applying scanning electron microscopy (SEM) measurements, as depicted in Fig. 2a–d. The images reveal SiO_2 plates with dimensions ranging from the submicron to the few-micron scale. Cu nanoparticles are homogeneously distributed

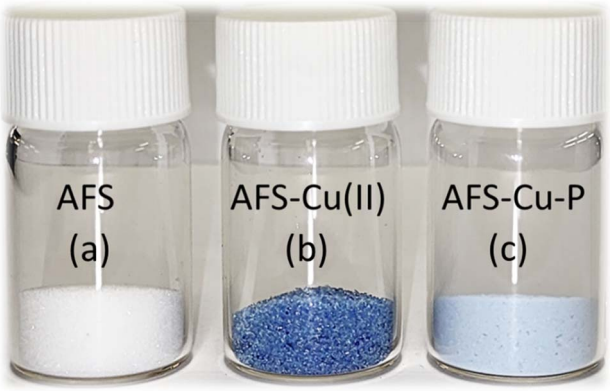

Fig. 1 Photographic image of the silica-modified with amine, AFS (a), AFS-Cu(II) (b) and AFS-Cu-P (c).

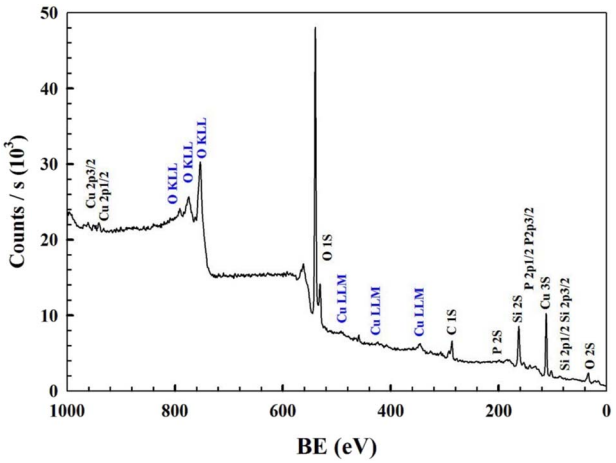

Fig. 3 XPS of the as-prepared AFS-Cu-P catalyst.

over the surface of silica. The elemental distribution over the catalyst surface is shown in ESI 1a. The detailed elemental composition was also obtained from the EDS measurements as shown in ESI 1b. The element Si is distributed over the entire surface of the catalyst, reflecting the large size of the silica plates. The Cu is homogeneously distributed over the silica plate, which agrees well with the SEM image. From the EDS measurements, the silicon content over the surface is high compared with the copper percentage. The elemental analysis (C, H & N) of the catalyst AFS-Cu-P shows the following percentages: 1.22, 0.651, and 6.40, respectively, while those for the original AFS and AFS-Cu(II) are 2.73, 1.33, and 6.19, and 1.16, 0.880, and 6.80, respectively. The carbon and hydrogen contents of the "parent" material AFS (without Cu) are relatively higher, whereas the N content is almost maintained in all three samples.

3.1.2. X-ray photoelectron spectroscopy (XPS). XPS measurements were conducted on the as-prepared AFS-Cu-P catalyst. Fig. 3 displays the XPS survey revealing copper, phosphorus, silicon, and oxygen in the catalyst. ESI 2 shows the XPS of these elements. The peaks at 930.5, 952.6, and 939.8 eV are assigned to Cu $2p_{3/2}$, Cu $2p_{1/2}$, and Cu L_2VV, respectively, as previously mentioned in the literature.[65,66] The peak appearing at 97.5 eV is assigned to Si $2p_{3/2}$, and a previously published work cited the peak at 98.80 eV.[67] The oxygen O 1s was observed

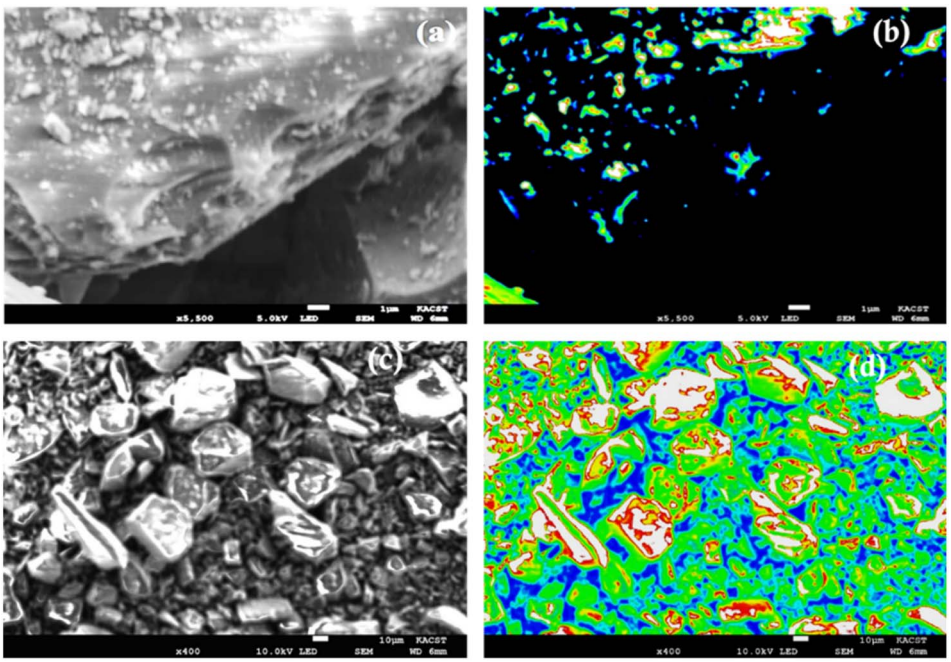

Fig. 2 (a) Surface morphology showing SiO_2 plates covered with nanostructured Cu particles for AFS-Cu-P. (b) Backscattering phase mapping of the Cu nanoparticle inclusion on the surface of the SiO_2 plates. (c) SEM image of the general distribution of the catalyst over the surface. (d) Phase mapping showing the different regions containing silicon and copper on the surface.

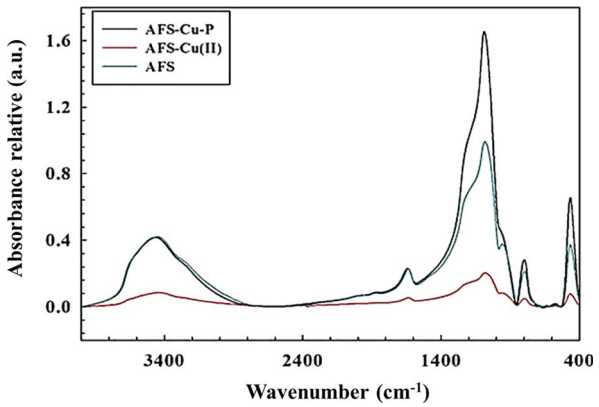

Fig. 4 FTIR spectra of as-prepared AFS-Cu-P, AFS-Cu(II), and AFS.

at 531.5 eV, which is reasonably consistent with the value mentioned earlier.[68] Two earlier reports showed that the P $2p_{3/2}$ peak appeared at 129.4 eV or 130.9 eV,[69,70] which were close to the values of 128.5 eV and 131.8 eV presented in this study.

3.2. Thermal gravimetric analysis

The thermal stability of the presented catalyst is of prime importance when applied in operational fields. The TGA profile of the as-prepared AFS-Cu-P catalyst is presented in ESI 3. Although the prepared catalyst will be applied as an electrode modifier for water splitting, it is not expected to be used at relatively high temperatures. However, from a practical point of view, it is essential to observe the response of the catalyst to temperature change. Compared to the standard support materials, AFS and the catalyst AFS-Cu-P show initial temperature stability with relatively lower weight loss as the temperature reaches 100 °C. This is apparently due to humidity expelled from the structure, whereas for the reference materials, the weight loss is relatively higher, indicating the loss of some of the compositional ingredients. All materials showed relatively lower weight loss of approximately 5% as the temperature rose from 100 °C to 800 °C, indicating relative stability with preservation of the chemical structure of the catalyst.

3.3. FTIR spectra

The FTIR spectra of the as-prepared catalyst, AFS-Cu-P, and the two reference materials, AFS-Cu(II) and AFS, are shown in Fig. 4. For the three materials, the structure of amorphous SiO_2 is confirmed. The following absorption bands can be identified: strong bands at 475 cm^{-1}, 801 cm^{-1}, and 1098 cm^{-1} are assigned to the asymmetric and symmetric Si–O–Si stretching vibrations.[71] The band at 1644 cm^{-1} and the broad band at 3475 cm^{-1} are assigned to the bending and stretching vibration modes of the O–H group. Furthermore, the bands at 3300 and 3500 cm^{-1} indicate that the silane agent *N*-(3-(trimethoxysilyl) propyl)ethylenediamine was successfully attached to the silica surface.[72,73]

3.4. Electrochemical characterization

3.4.1. Evaluation of different catalysts for water electrochemical splitting. Several catalysts have been used for the electrochemical splitting of water with the main goal of generating oxygen and hydrogen gasses.[74] The production of oxygen and hydrogen gasses through the electrolysis process results in high gas purity. However, reliable electrocatalysts for water splitting should fulfill several requirements, including long-term stability, low cost, and high efficiency. As previously described in the Experimental section, the catalyst is prepared using a simple procedure with a well-defined structure. The linear sweep voltammetry behavior of a glassy carbon electrode modified with the catalyst was compared in 1.0 M KOH in the presence of 0.33 M hydrazine using the following: GC, GC/CNT-AFS, GC/CNT-AFS-Cu(II), and GC/CNT-AFS-Cu-P electrodes. It is also important to compare the electrochemical behavior of these surfaces in the absence of hydrazine (*cf.* ESI 5). The data in Fig. 5 indicate that the onset of the oxygen evolution potential follows the order GC/CNT-AFS-Cu-P < GC/CNT-AFS-Cu(II) < GC/CNT-AFS < GC. The corresponding onset potentials followed the same order: 0.291 V, 0.379 V, 0.437 V, and 0.543 V (*vs.* RHE).

Also, as can be observed from the data, the current value increases in the same order for the surfaces studied. This indicates that the expected yield of oxygen evolution increases accordingly and follows the same order as the onset potentials. The use of Cu-containing catalysts results in enhanced electrochemical behavior, which decreases as the catalyst is deprived of phosphorous. ESI 5 depicts the linear sweep voltammogram of the different catalysts in 1.0 M KOH and in the absence of hydrazine. The specific current density values are relatively much lower compared with the case of the presence of hydrazine, with the GC/CNT-AFS-Cu-P electrode displaying the lowest onset potential, as expected. These data confirm the higher catalytic effect of the GC/CNT-AFS-Cu-P electrode compared with the other electrodes with an onset potential for oxygen evolution of 0.845 V. It is concluded that a lowering of the onset potential for oxygen evolution with a value of 0.554 V

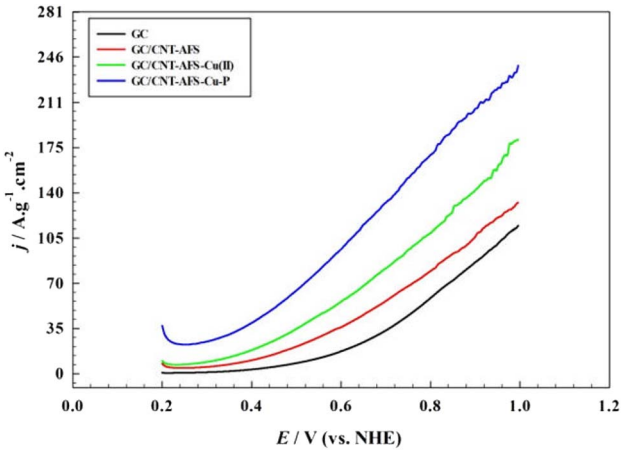

Fig. 5 Comparison of linear sweep voltammograms of different electrodes in 0.50 M KOH in the presence of 0.33 M hydrazine.

is achieved when using the GC/CNT-AFS-Cu-P electrode in the presence of hydrazine and with a value of 0.285 V compared with the bare GC surface (*cf.* ESI 6).

A previous study showed the following mechanisms for the electrochemical/chemical reactions for hydrazine oxidation as given in the diagram below:[75]

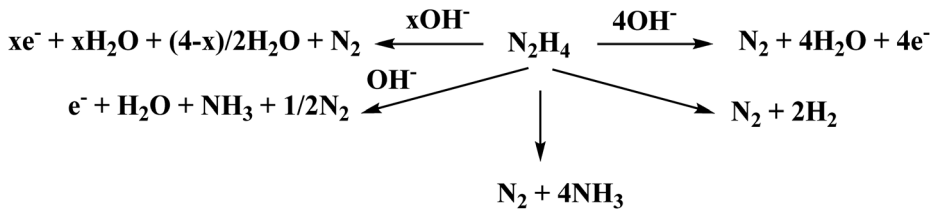

Thus, the silica surface acted as a support for Cu, allowing better exposure of the metal and its homogeneous distribution over the surface, consequently enhancing the charge transfer resistance and promoting the oxygen evolution reaction. According to Scheme 1 and the color photograph showing the real colors of the different materials, the distinct colors of amine silica bonded to copper ions prove the presence of the copper-complex distributed over the amine silica substrate. Therefore, it is advisable to investigate the performance of the GC/CNT-AFS-Cu-P electrode in detail. The CNT supported the catalyst to ensure its homogeneous distribution over the GC surface without sacrificing electrical conduction.

3.4.2. Optimization of the performance of GC/CNT-AFS-Cu-P for the OER. It is of prime importance to optimize the catalytic performance of the modified surface upon changing vital parameters, as described below. The effect of the amount of catalyst (AFS-Cu-P) applied for the modification of the surface of the electrode (GC) is depicted in Fig. 6. The amount loaded varied according to the volume that contained the catalyst and was added to the surface of the GC substrate. The results show that as the catalyst concentration rises, the onset potential for oxygen evolution falls. Furthermore, the specific current density rises with the catalyst concentration; when urea was applied over Ni-based catalysts, the outcomes were consistent with earlier research.[13] Thus, the number of electroactive sites increases, and the specific current density is enhanced as the amount of applied catalyst is increased. The amounts in grams of the catalyst were 5.0×10^{-6} g, 1.0×10^{-5} g, 5.0×10^{-5} g, and 1.0×10^{-4} g, when applying 10 μL, 20 μL, 50 μL, and 100 μL of the catalyst layers from the suspension, respectively.

We compared the solvent in which the catalyst was dissolved prior to its application to the substrate; the data in Fig. 6 shows the linear sweep voltammogram of the catalyst dissolved in a mixture of alcohol and Nafion (when applying 50 μL of the catalyst suspension) compared with that dissolved in dimethyl formamide. While the onset potential for oxygen evolution is comparable, the specific current density for the catalyst dissolved in the alcohol/Nafion mixture displays relatively higher values in lower potential ranges. However, we noticed that the surface modified with a catalyst dissolved in the alcohol/Nafion mixture exhibited less stability than the GC substrate.

Variation in the hydrazine concentration was found to impact both the onset potential and specific current density in the oxygen evolution reaction, as demonstrated in ESI 7. It is feasible to utilize hydrazine concentrations of up to 0.5 M in conjunction with 0.5 M KOH. Nevertheless, it is crucial to reduce the level of chemicals utilized in the electrolysis procedure. Moreover, it is important to minimize the concentration of chemicals employed during the electrolysis process. Therefore, with an optimized amount of catalyst over the GC substrate, the optimum concentration used during the electrolysis process will be limited to 0.33 M hydrazine. We calculated the "electro-active surface area" by running the cyclic voltammograms for the electrodes loaded with different amounts of the catalyst. In brief, each electrode with a given loading was tested in 1.0 mM $K_3[Fe(CN)_6]$ solution at different scan rates, as indicated in Fig. 6. From the plot of square root of the scan rate and peak current and knowing the value of the diffusion coefficient (D), the electroactive surface area was calculated using the Randles–Ševčík equation. The details of the experiment are mentioned elsewhere.[76] The calculated surface areas are as follows: for the 10 μL catalyst loading, the electro-active surface area is 0.017 cm^2; for the 50 μL catalyst loading, the electro-active surface area is: 0.558 cm^2; for the 100 μL catalyst loading, the electro-active surface area is 0.868 cm^2. The results confirm that as the amount of loaded catalyst increases over the electrode surface, the electroactive surface area increases, which results in the increase in the observed specific currents.

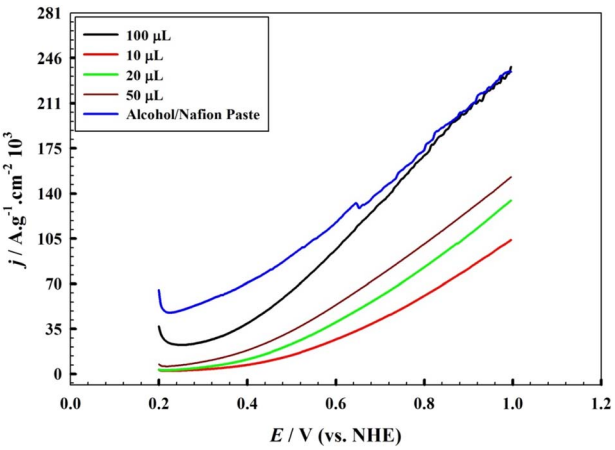

Fig. 6 Effect of the amount of catalyst (AFS-Cu-P) applied for the modification of the GC electrode. LSV with scan rate 10 mV s^{-1} in 0.33 M hydrazine/1.0 M KOH.

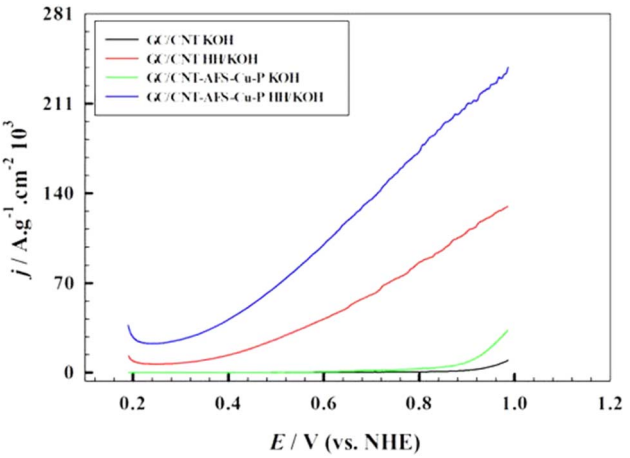

Fig. 7 Effect of adding multiwalled carbon nanotubes to the AFS-Cu-P catalyst on the linear sweep voltammogram in the presence and absence of hydrazine in 1.0 M KOH. Scan rate: 10 mV s^{-1}.

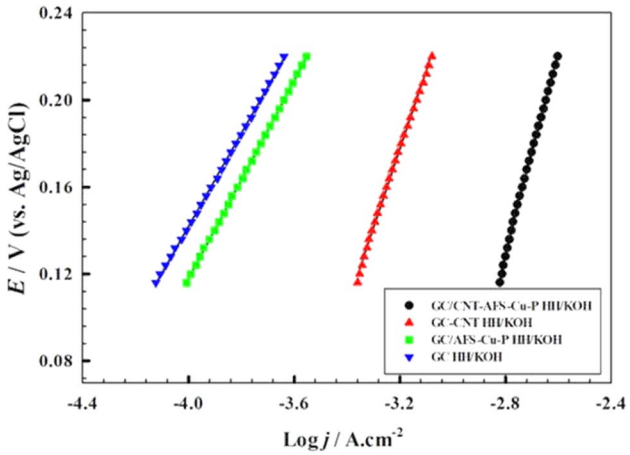

Fig. 8 Tafel plots for different electrodes in 0.33 M hydrazine and 1.0 M KOH. Scan rate: 1 mV s^{-1}.

In this respect, the effect of changing the concentration of KOH in the electrolysis process was evaluated while keeping the concentration of hydrazine constant. As illustrated in ESI 8, changing the KOH : hydrazine ratio had an impact on the oxygen evolution reaction onset potential and specific current density. The aspect ratio for the application of hydrazine to improve the oxygen evolution process was maintained at 3 : 1 for KOH:hydrazine.

The use of a carbon-based material as a substrate further improves the efficiency of the catalyst. In this regard, the support chosen was multi-walled carbon nanotubes, which were employed to investigate whether a more uniform dispersion of the catalyst would lead to an increased catalytic current for oxygen evolution. Fig. 7 displays the linear sweep voltammogram of the GC/CNT-AFS-Cu-P electrode both with and without hydrazine, with 1.0 M KOH serving as the supporting electrolyte. The results indicate that the use of CNT showed similar behavior compared to the case of using the catalyst under the same experimental conditions. The onset potential for oxygen evolution and the specific current densities did not change appreciably in this case. However, as indicated in the results of Fig. 7, using CNT only on the surface resulted in some catalytic activity toward the oxygen evolution reaction.

To study the details of the electrochemical kinetics of the oxygen evolution process, it was advisable to compare the results in the presence and absence of CNT with the catalyst.

3.5. Electrochemical kinetic study

3.5.1. Tafel measurements. At this stage, we assessed the electrochemical efficiency of various electrodes in relation to the oxygen evolution process by analyzing the potential/current correlation recorded within the extended quasi-equilibrium potential range. The applied voltage was greater than the oxygen evolution reaction's onset potential by +100 mV. The studied electrodes were GC, GC/CNT, GC/GC/AFS-Cu-P, and GC/CNT-AFS-Cu-P. The electrolyte was 0.33 M hydrazine in 1.0 M KOH. The Tafel plots of the different electrodes are shown in Fig. 8.

Table 1 Tafel parameters for different electrodes and different modifiers in 0.33 M hydrazine/1.0 M KOH

Surface	α	$J_\circ$ /A cm^{-2}
GC	0.931	2.17×10^{-5}
GC/CNT	0.959	2.05×10^{-4}
GC/AFS@100 Phos-Cu	0.935	3.04×10^{-5}
GC/CNT-AFS@100 Phos-Cu	0.968	8.38×10^{-4}

The Tafel slopes were 213 mV dec^{-1}, 360 mV dec^{-1}, 227 mV dec^{-1}, and 467 mV dec^{-1} for the GC, GC/CNT, GC/GC/AFS-Cu-P, and GC/CNT-AFS-Cu-P, respectively. Previous reports have indicated that the Tafel slopes varied according to the type of catalyst used for the oxygen evolution reaction and whether the medium was basic or acidic. Thus, uncommonly low Tafel slopes, ranging between 28 mV dec^{-1} and 35 mV dec^{-1} have been reported for NiFe-, Ni-, and Co-based catalysts.[13,14,77,78] Higher values of Tafel slopes have been reported for other catalysts, including perovskite-based catalysts such as $LnBaCo_2O_{5+n\delta}$, $NiCo_2O_4$, and CoPi.[15,78–80] The charge transfer coefficients and corresponding exchange current densities are listed in Table 1. The Tafel slope helps to explain the reaction mechanism, while the exchange current density defines the catalytic activity of the surface toward the process.[81,82] Therefore, from the data in Table 1 and the aforementioned values of the Tafel slopes of the different surfaces studied in this work, the incorporation of CNT into the catalyst structure enhances the catalytic activity toward the oxygen evolution reaction. Therefore, the activation energy of the oxygen evolution reaction is lowered and charge exchange at the interface is facilitated.

The transfer coefficients α reported in Table 1 are relatively high and describe the irreversible nature of the electrochemical oxygen evolution reaction. Relatively lower values for the transfer coefficients have been reported earlier for different

processes.[83,84] The force constants of the oxidized and reduced components of the process determine the value of the transfer coefficient for a redox process, as Marcus explained in prior work.[85] For example, the values of α are likely to deviate from the ideal symmetric value of 0.5 if the force constants are not balanced and if the reacting species are adsorbed at the surface of the catalytic sites during the electron transfer process;[86] this situation may occur in the case of the present catalysts. The "basic" Tafel relationship can been given as follows:

$$\eta = a + a\log(j) \tag{2}$$

From the empirical relationship of eqn (2), the exchange current density, charge transfer coefficient, and Tafel slope are derived. In this relationship, η is the overpotential imposed on the electrode and b is the slope. The Butler–Volmer equation and its derived version describe reversible electrochemical redox processes[87] as follows:

$$j = J_{\circ}\{\exp(-\alpha f\eta) - \exp[(1-\alpha)f\eta]\} \tag{3}$$

$$\eta = \frac{\mathrm{RT}}{\alpha F}\ln(j_{\circ}) - \frac{\mathrm{RT}}{\alpha F}\ln(j) \tag{4}$$

The transfer coefficient in these equations is denoted by α, and f is equal to F/RT (where F is the universal gas constant, T is the absolute temperature, and j_0 is the exchange current density). Eqn (4) is the equivalent of eqn (2) when the forward (oxidation) or reverse (reduction) reaction is taken into account.

The electron transfer coefficients are also derived from the Tafel relationship. For the rate-determining stage of the electrode reaction, the following relationship can be used to estimate the electron transfer coefficient, α_a:[88]

$$\alpha_a = \left(\frac{\mathrm{RT}}{nF}\right)\left(\frac{\mathrm{d}\ln\ j_a}{\mathrm{d}E}\right) \tag{5}$$

In eqn (5), the term ($\mathrm{d}E/\mathrm{d}\ln j_a$) is the anodic Tafel slope, n is the number of electrons taken up by the electrode, and the other terms assume their commonly recognized definitions. The oxygen evolution reaction is known for its complexity, and previous studies have suggested that the reaction proceeds either through two- or four-electron reaction mechanisms, as described for a metal site M, where each step of these reactions is considered as a rate-determining step:[89–92]

$$\mathrm{M} + \mathrm{OH}^- \rightleftarrows \mathrm{MOH} + \mathrm{e}^- \tag{6}$$

$$\mathrm{MOH} + \mathrm{OH}^- \rightleftarrows \mathrm{MO} + \mathrm{H_2O} + \mathrm{e}^- \tag{7}$$

$$\mathrm{MO} + \mathrm{OH}^- \rightleftarrows \mathrm{MOOH} + \mathrm{e}^- \tag{8}$$

$$\mathrm{MOOH} + \mathrm{OH}^- \rightleftarrows \mathrm{MOO}^- + \mathrm{H_2O} \tag{9}$$

$$\mathrm{MOO}^- \rightleftarrows \mathrm{M} + \mathrm{O_2} + \mathrm{e}^- \tag{10}$$

3.5.2. Diffusion coefficient and reaction rate constant. Chronoamperometry measurements were conducted on different catalysts to determine the apparent diffusion coefficients (D) and rate constants (k) for the oxygen evolution reaction in the presence of hydrazine in an alkaline medium. We used previously adopted relationships to determine the values of the apparent diffusion coefficients (D) and rate constants (k):[93,94]

$$I_p = nFAC{\cdot}D^{1/2}(\pi)^{-1/2}(t)^{-1/2} \tag{11}$$

$$I_C/I_L = \pi^{1/2}(kct)^{1/2} \tag{12}$$

The terms in eqn (11) and (12) are defined as follows: I_p is the specific oxidation current density of the catalytic process, A is the electrode area, $C_{\circ}$ is the concentration of hydrazine, I_L is the current density value in the absence of hydrazine, and I_C is the current density value in the presence of hydrazine. The other terms assume the following regular definitions: n is the number of electrons exchanged during the catalytic process, F is Faraday's constant, t is the time, D is the apparent diffusion coefficient ($\mathrm{cm^2\ s^{-1}}$) and k is the catalytic rate constant ($\mathrm{cm^3\ mol^{-1}\ s^{-1}}$).

From eqn (11), a plot of I_p *versus* $t^{-1/2}$ can be prepared and the values of the diffusion coefficients (D) can be estimated for the studied electrodes. Fig. 9a shows the chronoamperometry experiments using the following electrodes: GC, GC/CNT, GC/GC/AFS-Cu-P, and GC/CNT-AFS-Cu-P in 0.33 M hydrazine/1.0 M KOH. The constant potentials applied to the electrodes were derived from the corresponding linear sweep voltammogram at the corresponding onset potentials for the oxygen evolution reaction (*cf.* Fig. 5). The current values display distinct values as the time span reaches 300 s, where a steady state of the process is reached. The observed values of the "steady-state" current are in the following order: GC/CNT-AFS-Cu-P > GC/CNT > GC/GC/AFS-Cu-P ≈ GC.

Therefore, most kinetic changes occur during the initial moments of the chronoamperograms. It is also concluded that the charge transfer process is controlled by activation. The evidence that determines this possibility is the effect of the scan rate on the linear sweep voltammogram, as shown in ESI 9. No appreciable changes in the onset potential for the oxygen evolution reaction were observed with close values of the specific current densities.

Fig. 9b displays the relationship between the specific oxidation current densities *vs.* $t^{-1/2}$ for the different studied electrodes in 0.33 M hydrazine/1.0 M KOH. From eqn (11), the apparent diffusion coefficients are calculated and are listed in Table 2. The apparent diffusion coefficient increases in the following order for the electrodes: GC/CNT-AFS-Cu-P > GC/CNT > GC/GC/AFS-Cu-P > GC. This again indicates the effect of employing CNTs on the structure of the catalyst. The steady-state currents indicate the high efficiency of the surface when incorporating the CNT.

Fig. 9c shows the relationship between the oxidation current ratios and $t^{1/2}$ in the presence and absence of hydrazine. Using eqn (12), the values of the rate constants k are calculated and are displayed in Table 2. Again, the values of k are in the same order as the diffusion coefficients, emphasizing the crucial role

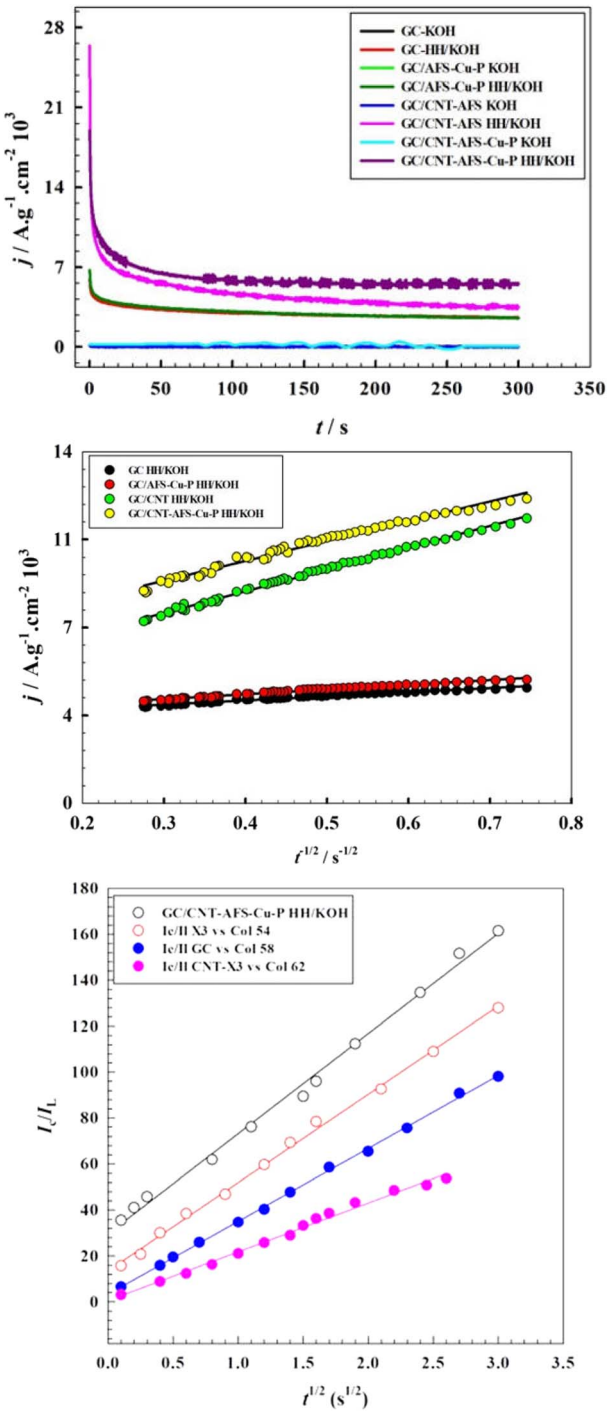

Fig. 9 (a) Chronoamperometry measurements over different electrodes in 1.0 M KOH and 0.33 M hydrazine/1.0 M KOH. (b) Relationship between catalytic specific oxidation current densities (j) *versus* $t^{-1/2}$ for different electrodes in 0.33 M hydrazine/1.0 M KOH. (c) Relationship between catalytic specific oxidation current density ratio *versus* $t^{1/2}$ for different electrodes in the presence and absence of 0.33 M hydrazine/1.0 M KOH.

played by the CNTs incorporated in the catalyst. The performance of the present electrode modified with the catalyst (CNT-AFS-Cu-P) was compared to those of some recently reported copper-based and other catalysts. The figures of merit are listed in ESI 10.[95–103]

Table 2 Apparent diffusion coefficient D and catalytic rate constant values k for the oxygen evolution reaction in 0.33 M hydrazine/1.0 M KOH

Electrode	k (mol^{-1} L s^{-1})	D (cm^2 s^{-1})
GC	4.28×10^5	5.66×10^{-8}
GC/GC/AFS-Cu-P	9.75×10^5	8.22×10^{-7}
GC/CNT	1.09×10^6	6.81×10^{-5}
GC/CNT-AFS-Cu-P	3.41×10^6	8.87×10^{-5}

3.6. Electrochemical impedance spectroscopy (EIS)

To understand the interfacial interactions at the electrode/electrolyte interface, EIS experiments were conducted. The measurements compared the GC/GC/AFS-Cu-P and GC electrodes in 0.33 M hydrazine/1.0 M KOH. The applied dc voltage to each electrode was determined from the onset potential of the oxygen evolution reaction, as described in linear sweep voltammetry. The data in Fig. 10 show the Nyquist plots and the fitted data using the equivalent circuit in the inset of the figure. For both electrodes, the data are in the form of a semicircle that can be simulated using a simple Randles circuit. The values of the circuit elements are given in Table 3. The charge transfer resistance represents the extent of the barrier imposed on the charge exchange at the interface. The radius of the semicircle in the Nyquist plot is representative of the value of R_{ct}. The elements of the circuit are as follows: R_s is the solution resistance; R_{ct}, the charge transfer resistance; and Y_o, the surface roughness of the catalyst. The catalytic activity of the GC/GC/

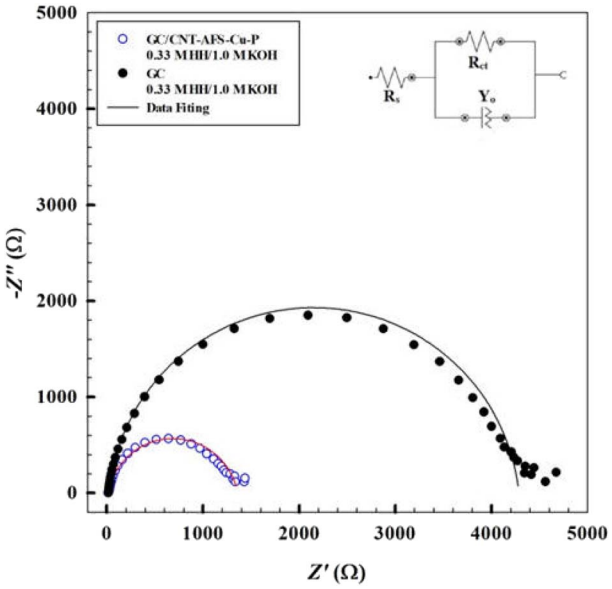

Fig. 10 Nyquist plots of the GC and GC/GC/AFS-Cu-P electrodes in 0.33 M hydrazine/1.0 M KOH. The symbols represent the data, and the solid lines represent the data fit. The corresponding circuit is shown in the inset.

Table 3 EIS data extracted from the data fitting of the results of Fig. 10

Element	GC/CNT-AFS@100 Phos-Cu GC/GC/AFS-Cu-P	GC
R_s (Ω)	16.5	17.8
R_{ct} (Ω)	1344	4267
Y_0 (μMho.s^n)	6.35×10^{-5}	6.28×10^{-6}
n	0.893	0.937
χ^2	0.0893	0.0604

AFS-Cu-P electrode was higher than that of the unmodified GC. The capacitance of the surface is slightly higher for the modified surface than for the GC electrode.

3.6.1. Catalyst stability. We conducted two types of tests to evaluate the stability of the electrode modified with the catalysts. In the first, the electrode was subjected to repeated linear sweep voltammetry (LSV) experiments twenty-five successive times. The electrolyte was 0.50 M KOH in the presence of 0.33 M hydrazine with a scan rate of 10 mV s^{-1}. The figure of ESI 11a shows the repeated LSVs. The arrows at points A, B, C and D show the change in specific currents at four different potential values: 0.4 V, 0.6 V, 0.8 V and 1.0 V. The decrease in current values was found to be 18.0%, 19.7%, 21.4% and 23.6%, respectively.

The second experiment was to expose the electrode modified with the catalyst to a constant applied potential of 0.05 V in 0.33 M hydrazine/1.0 M KOH for an extended time of one hour. The experiment was repeated at two-day intervals, and the chronoamperometry diagrams were recorded. The figure of ESI 11b shows the results.

The results for each day show good stability over the exposure time of one hour. The day-to-day data show closely similar data with average specific current variations of 7.2%. The results from the LSVs and CAs confirm the stability of the electrode performance under the given electrolytic conditions.

4 Conclusions

In this study, we prepared a series of catalysts@silica to evaluate their performance in electrolytic water splitting in a basic medium. The employment of hydrazine in the medium assisted the process of the OER both thermodynamically and kinetically. Among the electrodes used, GC/AFS-Cu-P showed the lowest onset OER overpotential. The presence of copper and CNT in the composition of the catalyst resulted in relatively higher specific current densities and a decrease in the overpotential values. The complex formation of Cu with phosphorus proved crucial for the electrolytic splitting of water, as deduced from the kinetic parameters. The kinetic parameters based on the Tafel slopes and apparent rate constants showed that the presence of CNT as a matrix to support the catalyst is crucial for the process. The observed rate constants and diffusion coefficients for the GC/GC/AFS-Cu-P electrode were as high as 3.41×10^6 mol^{-1} L s^{-1} and 8.87×10^{-5} cm^2 s^{-1}, respectively. The relatively high Tafel slopes reflected the irreversibility of the process, and the effectiveness of the catalyst was reflected by the high exchange current densities obtained.

Data availability

The data that support the findings of this study, "Cu-P@silica-CNT-based catalyst for effective electrolytic water splitting in an alkaline medium with hydrazine assistance," are available on request.

Conflicts of interest

The authors declare no conflict of interest.

Acknowledgements

The authors would like to extend their gratitude to the King Abdulaziz City for Science and Technology (KACST) for their assistance in providing logistical and technical support.

References

1 A. Kumar, P. Sharma, G. Sharma, P. Dhiman, M. Shekh, M. Sillanpää and F. J. Stadler, Recent progress in advanced strategies to enhance the photocatalytic performance of metal molybdates for H2 production and CO2 reduction, *J. Alloys Compd.*, 2024, **971**, 172665, DOI: 10.1016/j.jallcom.2023.172665.

2 D. Agrawal, N. Mahajan, S. A. Singh and I. Sreedhar, Green hydrogen production pathways for sustainable future with net zero emissions, *Fuel*, 2024, **359**, 130131, DOI: 10.1016/j.fuel.2023.130131.

3 N. Rahamathulla, N. Vadivel, J. Theerthagiri, R. S. Raj, C. J. Moon, A. P. Murthy, S. Kheawhom and M. Y. Choi, Underlying aspects of surface amendment strategies adopted in electrocatalysts for overall water splitting under alkaline conditions, *Curr. Opin. Electrochem.*, 2024, **43**, 101428, DOI: 10.1016/j.coelec.2023.101428.

4 Y. Wan, L. Zhou and R. Lv, Rational design of efficient electrocatalysts for hydrogen production by water electrolysis at high current density, *Mater. Chem. Front.*, 2023, **7**, 6035–6060, DOI: 10.1039/d3qm00722g.

5 J. Durst, C. Simon, F. Hasché and H. A. Gasteiger, Hydrogen Oxidation and Evolution Reaction Kinetics on Carbon Supported Pt, Ir, Rh, and Pd Electrocatalysts in Acidic Media, *J. Electrochem. Soc.*, 2015, **162**, F190–F203, DOI: 10.1149/2.0981501jes.

6 R. Subbaraman, D. Tripkovic, K. C. Chang, D. Strmcnik, A. P. Paulikas, P. Hirunsit, M. Chan, J. Greeley, V. Stamenkovic and N. M. Markovic, Trends in activity for the water electrolyser reactions on 3d M(Ni,Co,Fe,Mn) hydr(oxy)oxide catalysts, *Nat. Mater.*, 2012, **11**, 550–557, DOI: 10.1038/nmat3313.

7 J. Suntivich, K. J. May, H. A. Gasteiger, J. B. Goodenough and Y. Shao-Horn, A perovskite oxide optimized for oxygen evolution catalysis from molecular orbital principles, *Science*, 2011, **334**, 1383–1385, DOI: 10.1126/science.1212858.

8 J. K. Nørskov, J. Rossmeisl, A. Logadottir, L. Lindqvist, J. R. Kitchin, T. Bligaard and H. Jónsson, Origin of the Overpotential for Oxygen Reduction at a Fuel-Cell Cathode, *J. Phys. Chem. B*, 2004, **108**, 17886–17892, DOI: 10.1021/jp047349j.

9 J. S. Spendelow and A. Wieckowski, Electrocatalysis of oxygen reduction and small alcohol oxidation in alkaline media, *Phys. Chem. Chem. Phys.*, 2007, **9**, 2654–2675, DOI: 10.1039/b703315j.

10 Z. Tianhou and A. B. Anderson, Hydrogen oxidation and evolution on platinum electrodes in base: Theoretical study, *J. Phys. Chem. C*, 2007, **111**, 8644–8648, DOI: 10.1021/jp070125r.

11 J. J. T. T. Vermeijlen, L. J. J. Janssen and G. J. Visser, Mechanism of hydrogen oxidation on a platinum-loaded gas diffusion electrode, *J. Appl. Electrochem.*, 1997, **27**, 497–506, DOI: 10.1023/A:1018434325530.

12 S. Ernst and C. H. Hamann, The pH-dependence of the hydrogen exchange current density at smooth platinum in alkaline solution (KOH), *J. Electroanal. Chem.*, 1975, **60**, 97–100, DOI: 10.1016/S0022-0728(75)80206-3.

13 H. K. Srour, N. F. Atta, M. W. Khalil and A. Galal, Ionic liquid crystals/nano-nickel oxide-decorated carbon nanotubes composite for electrocatalytic treatment of urea-contaminated water, *J. Water Process Eng.*, 2022, **48**, 102823, DOI: 10.1016/j.jwpe.2022.102823.

14 Z. Lu, W. Xu, W. Zhu, Q. Yang, X. Lei, J. Liu, Y. Li, X. Sun and X. Duan, Three-dimensional NiFe layered double hydroxide film for high-efficiency oxygen evolution reaction, *Chem. Commun.*, 2014, **50**, 6479–6482, DOI: 10.1039/c4cc01625d.

15 H. Shi and G. Zhao, Water Oxidation on Spinel NiCo 2 O 4 Nanoneedles Anode: Microstructures, Specific Surface Character, and the Enhanced Electrocatalytic Performance, *J. Phys. Chem. C*, 2014, **118**, 25939–25946, DOI: 10.1021/jp508977j.

16 P. Zhou, L. Wu, Z. Ji, C. Fan, X. Shen, G. Zhu and L. Xu, Construction of NiFe(CN)5NO/Ni3S2 hierarchical submicro-rods on nickel foam as advanced oxygen evolution electrocatalysts, *J. Colloid Interface Sci.*, 2023, **646**, 98–106, DOI: 10.1016/j.jcis.2023.05.032.

17 L. Chen, Y. Yang, S. Jiang, B. Yang and W. Rao, Multifunctional ferroelectric catalysis for water splitting: classification, synergism, strategies and challenges, *Mater. Today Chem.*, 2023, **30**, 101486, DOI: 10.1016/j.mtchem.2023.101486.

18 Z. Feng, P. Wang, Y. Cheng, Y. Mo, X. Luo, P. Liu, R. Guo and X. Liu, Recent progress on NiFe2O4 spinels as electrocatalysts for the oxygen evolution reaction, *J. Electroanal. Chem.*, 2023, **946**, 117703, DOI: 10.1016/j.jelechem.2023.117703.

19 J. Zhao, J. J. Zhang, Z. Y. Li and X. H. Bu, Recent Progress on NiFe-Based Electrocatalysts for the Oxygen Evolution Reaction, *Small*, 2020, **16**, 2003916, DOI: 10.1002/smll.202003916.

20 Y. Wang, L. Wang, K. Zhang, J. Xu, Q. Wu, Z. Xie, W. An, X. Liang and X. Zou, Electrocatalytic water splitting over perovskite oxide catalysts, *Chin. J. Catal.*, 2023, **50**, 109–125, DOI: 10.1016/S1872-2067(23)64452-3.

21 A. M. K. Fehr, T. G. Deutsch, F. M. Toma, M. S. Wong and A. D. Mohite, Technoeconomic Model and Pathway to <$2/kg Green Hydrogen Using Integrated Halide Perovskite Photoelectrochemical Cells, *ACS Energy Lett.*, 2023, **8**, 4976–4983, DOI: 10.1021/acsenergylett.3c01865.

22 X. Wang, Y. Peng, S. Yang, H. G. Yang and Y. Hou, Recent progress in metal halide perovskite photocatalysts for hydrogen evolution, *Mater. Chem. Front.*, 2023, **7**, 4635–4657, DOI: 10.1039/d3qm00477e.

23 H. Zhao and Z. Yuan, Progress and Perspectives for Solar-Driven Water Electrolysis to Produce Green Hydrogen, *Adv. Energy Mater.*, 2023, **13**, 2300254, DOI: 10.1002/aenm.202300254.

24 H. A. Centurion, M. A. Melo, L. G. Rabelo, G. A. S. Alves, W. S. Rosa, I. Rodríguez-Gutiérrez, F. L. Souza and R. V. Gonçalves, Emerging trends of pseudobrookite Fe2TiO5 photocatalyst: A versatile material for solar water splitting systems, *J. Alloys Compd.*, 2023, **933**, 167710, DOI: 10.1016/j.jallcom.2022.167710.

25 N. F. Khusnun, A. Arshad, A. A. Jalil, L. Firmansyah, N. S. Hassan, W. Nabgan, A. A. Fauzi, M. B. Bahari, N. Ya'aini, A. Johari and R. Saravanan, An avant-garde of carbon-doped photoanode materials on photo-electrochemical water splitting performance: A review, *J. Electroanal. Chem.*, 2023, **929**, 117139, DOI: 10.1016/j.jelechem.2022.117139.

26 W. J. Dong and Z. Mi, One-dimensional III-nitrides: towards ultrahigh efficiency, ultrahigh stability artificial photosynthesis, *J. Mater. Chem. A*, 2023, **11**, 5427–5459, DOI: 10.1039/d2ta09967e.

27 M. Ashraf, N. Ullah, I. Khan, W. Tremel, S. Ahmad and M. N. Tahir, Photoreforming of Waste Polymers for Sustainable Hydrogen Fuel and Chemicals Feedstock: Waste to Energy, *Chem. Rev.*, 2023, **123**, 4443–4509, DOI: 10.1021/acs.chemrev.2c00602.

28 K. Prakash, B. Mishra, D. D. Díaz, C. M. Nagaraja and P. Pachfule, Strategic design of covalent organic frameworks (COFs) for photocatalytic hydrogen generation, *J. Mater. Chem. A*, 2023, **11**, 14489–14538, DOI: 10.1039/d3ta02189k.

29 S. Keshipour and F. Eyvari-Ashnak, Nitrogen-Doped Electrocatalysts, and Photocatalyst in Water Splitting: Effects, and Doping Protocols, *ChemElectroChem*, 2023, **10**, 202201153, DOI: 10.1002/celc.202201153.

30 D. Deepak, J. Raghav, A. Panghal, T. Singh, S. Roy and S. S. Roy, Hybrid framework of sputter deposited vanadium nitride embedded Cu2O/CuO nanostructures for electrocatalytic oxygen evolution reaction, *J. Alloys Compd.*, 2024, **978**, 173391, DOI: 10.1016/j.jallcom.2023.173391.

31 W. Du, Y. Feng, J. Jiang, T. Zhao, G. Xu and L. Zhang, Preparation of hollow nanorod CoxCu2−xSe/CF electrode assembled from nanoparticles and its urea-assisted hydrogen production performance, *J. Alloys Compd.*, 2024, **970**, 172517, DOI: 10.1016/j.jallcom.2023.172517.

32 J. Zhang, X. Liu, Y. Li, K. Zhang, X. Yang, H. Shi, D. Liu, X. Song, Z. Song and S. Li, In situ construction of a dendritic CuBi2O4/CuO heterojunction photocathode for overall water splitting, *J. Alloys Compd.*, 2024, **970**, 172575, DOI: 10.1016/j.jallcom.2023.172575.

33 J. Shen, Y. Liu, Q. Chen, W. Yu and Q. Zhong, In-situ construction defect-rich CuNiCoS4/1T-MoS2 heterostructures as superior electrocatalysts for water splitting, *J. Colloid Interface Sci.*, 2024, **658**, 1009–1015, DOI: 10.1016/j.jcis.2023.12.027.

34 P. Varma, L. Alvares Rodrigues, Y. Lianqing and D. A. Reddy, Role of active area on photoelectrochemical water-splitting performance of inverse opal CuBi2O4 photocathodes, *Appl. Surf. Sci.*, 2023, **624**, 157143, DOI: 10.1016/j.apsusc.2023.157143.

35 X. Mu, K. Wang, K. Lv, B. Feng, X. Yu, L. Li, X. Zhang, X. Yang and Z. Lu, Doping of Cr to Regulate the Valence State of Cu and Co Contributes to Efficient Water Splitting, *ACS Appl. Mater. Interfaces*, 2023, **15**, 16552–16561, DOI: 10.1021/acsami.2c18799.

36 J. Zhang, A. Bifulco, P. Amato, C. Imparato and K. Qi, Copper indium sulfide quantum dots in photocatalysis, *J. Colloid Interface Sci.*, 2023, **638**, 193–219, DOI: 10.1016/j.jcis.2023.01.107.

37 Z. Zhang, Z. Wang, H. Zhang, Z. Zhang, J. Zhou, Y. Hou, P. Liu, B. Xu, H. Zhang and J. Guo, Interface engineering of porous Co(OH)2/La(OH)3@Cu nanowire heterostructures for high efficiency hydrogen evolution and overall water splitting, *J. Mater. Chem. A*, 2023, **11**, 4355–4364, DOI: 10.1039/d2ta08571b.

38 J. Jiang, L. Wang, J. Zhu, Y. Yang, T. Wang, H. Tao, T. Wang and X. Dong, Self-supporting ZnO-Cu2S nanoflower arrays heterostructure with superhydrophilic and aerophobic properties for oxygen evolution reaction, *J. Alloys Compd.*, 2023, **960**, 170814, DOI: 10.1016/j.jallcom.2023.170814.

39 A. S. Mary, C. Murugan and A. Pandikumar, Uplifting the charge carrier separation and migration in Co-doped CuBi2O4/TiO2 p–n heterojunction photocathode for enhanced photoelectrocatalytic water splitting, *J. Colloid Interface Sci.*, 2022, **608**, 2482–2492, DOI: 10.1016/j.jcis.2021.10.172.

40 N. H. Khdary, M. A. Ghanem, M. E. Abdelsalam, D. N. Khdary and N. H. Alotaibi, Copper-N-SiO2 nanoparticles catalyst for hydrogen evolution reaction, *Int. J. Hydrogen Energy*, 2019, **44**, 22926–22935, DOI: 10.1016/j.ijhydene.2019.06.186.

41 Y. Wang, S. Li, D. Zhang, F. Tan, L. Li and G. Hu, Self-supported hierarchical P,Cu-codoped cobalt selenide nanoarrays for enhanced overall water splitting, *J. Alloys Compd.*, 2022, **889**, 161696, DOI: 10.1016/j.jallcom.2021.161696.

42 S. K. Das, A. Chowdhury, K. Bhunia, A. Ghosh, D. Chakraborty, M. Das, U. Kayal, A. Modak, D. Pradhan and A. Bhaumik, Ni(II) and Cu(II) grafted porphyrin-pyrene based conjugated microporous polymers as bifunctional electrocatalysts for overall water splitting, *Electrochim. Acta*, 2023, **459**, 142553, DOI: 10.1016/j.electacta.2023.142553.

43 T. Shinagawa, A. T. Garcia-Esparza and K. Takanabe, Insight on Tafel slopes from a microkinetic analysis of aqueous electrocatalysis for energy conversion, *Sci. Rep.*, 2015, **5**, 13801, DOI: 10.1038/srep13801.

44 J. Y. Zhang, H. Wang, Y. Tian, Y. Yan, Q. Xue, T. He, H. Liu, C. Wang, Y. Chen and B. Y. Xia, Anodic Hydrazine Oxidation Assists Energy-Efficient Hydrogen Evolution over a Bifunctional Cobalt Perselenide Nanosheet Electrode, *Angew. Chem., Int. Ed.*, 2018, **57**, 7649–7653, DOI: 10.1002/anie.201803543.

45 Z. Wang, L. Xu, F. Huang, L. Qu, J. Li, K. A. Owusu, Z. Liu, Z. Lin, B. Xiang, X. Liu, K. Zhao, X. Liao, W. Yang, Y. B. Cheng and L. Mai, Copper–Nickel Nitride Nanosheets as Efficient Bifunctional Catalysts for Hydrazine-Assisted Electrolytic Hydrogen Production, *Adv. Energy Mater.*, 2019, **9**, 1900390, DOI: 10.1002/aenm.201900390.

46 H. Liu, Y. Liu, M. Li, X. Liu and J. Luo, Transition-metal-based electrocatalysts for hydrazine-assisted hydrogen production, *Mater. Today Adv.*, 2020, **7**, 100083, DOI: 10.1016/j.mtadv.2020.100083.

47 C. Tang, R. Zhang, W. Lu, Z. Wang, D. Liu, S. Hao, G. Du, A. M. Asiri and X. Sun, Energy-Saving Electrolytic Hydrogen Generation: Ni2P Nanoarray as a High-Performance Non-Noble-Metal Electrocatalyst, *Angew. Chem., Int. Ed.*, 2017, **56**, 842–846, DOI: 10.1002/anie.201608899.

48 L. Wu, H. Dai, X. Wen and P. Wang, Ni–Zn Alloy Nanosheets Arrayed on Nickel Foamas a Promising Catalyst for Electrooxidation of Hydrazine, *ChemElectroChem*, 2017, **4**, 1944–1949, DOI: 10.1002/celc.201700234.

49 L. Zhu, J. Huang, G. Meng, T. Wu, C. Chen, H. Tian, Y. Chen, F. Kong, Z. Chang, X. Cui and J. Shi, Active site recovery and N-N bond breakage during hydrazine oxidation boosting the electrochemical hydrogen production, *Nat. Commun.*, 2023, **14**, 1997, DOI: 10.1038/s41467-023-37618-2.

50 Y. Liu, J. Zhang, Y. Li, Q. Qian, Z. Li, Y. Zhu and G. Zhang, Manipulating dehydrogenation kinetics through dual-doping Co3N electrode enables highly efficient hydrazine oxidation assisting self-powered H2 production, *Nat. Commun.*, 2020, **11**, 1853, DOI: 10.1038/s41467-020-15563-8.

51 H. Wang, Y. Ma, R. Wang, J. Key, V. Linkov and S. Ji, Liquid-liquid interface-mediated room-temperature synthesis of amorphous NiCo pompoms from ultrathin nanosheets with high catalytic activity for hydrazine oxidation, *Chem. Commun.*, 2015, **51**, 3570–3573, DOI: 10.1039/c4cc09928a.

52 H. Zhang, A. W. Maijenburg, X. Li, S. L. Schweizer and R. B. Wehrspohn, Bifunctional Heterostructured Transition Metal Phosphides for Efficient Electrochemical Water Splitting, *Adv. Funct. Mater.*, 2020, **30**, 2003261, DOI: 10.1002/adfm.202003261.

53 K. Zeng, X. Zheng, C. Li, J. Yan, J. H. Tian, C. Jin, P. Strasser and R. Yang, Recent Advances in Non-Noble Bifunctional Oxygen Electrocatalysts toward Large-Scale Production, *Adv. Funct. Mater.*, 2020, **30**, 2000503, DOI: 10.1002/adfm.202000503.

54 J. Si, Q. Zheng, H. Chen, C. Lei, Y. Suo, B. Yang, Z. Zhang, Z. Li, L. Lei, Y. Hou and K. Ostrikov, Scalable Production of Few-Layer Niobium Disulfide Nanosheets *via*

Electrochemical Exfoliation for Energy-Efficient Hydrogen Evolution Reaction, *ACS Appl. Mater. Interfaces*, 2019, **11**, 13205–13213, DOI: 10.1021/acsami.8b22052.

55 Q. Sun, L. Wang, Y. Shen, M. Zhou, Y. Ma, Z. Wang and C. Zhao, Bifunctional Copper-Doped Nickel Catalysts Enable Energy-Efficient Hydrogen Production *via* Hydrazine Oxidation and Hydrogen Evolution Reduction, *ACS Sustain. Chem. Eng.*, 2018, **6**, 12746–12754, DOI: 10.1021/acssuschemeng.8b01887.

56 Z. Pu, I. Saana Amiinu, F. Gao, Z. Xu, C. Zhang, W. Li, G. Li and S. Mu, Efficient strategy for significantly decreasing overpotentials of hydrogen generation *via* oxidizing small molecules at flexible bifunctional CoSe electrodes, *J. Power Sources*, 2018, **401**, 238–244, DOI: 10.1016/j.jpowsour.2018.08.085.

57 P. F. Yin, M. Zhou, J. Chen, C. Tan, G. Liu, Q. Ma, Q. Yun, X. Zhang, H. Cheng, Q. Lu, B. Chen, Y. Chen, Z. Zhang, J. Huang, D. Hu, J. Wang, Q. Liu, Z. Luo, Z. Liu, Y. Ge, X. J. Wu, X. W. Du and H. Zhang, Synthesis of Palladium-Based Crystalline@Amorphous Core–Shell Nanoplates for Highly Efficient Ethanol Oxidation, *Adv. Mater.*, 2020, **32**, 2000482, DOI: 10.1002/adma.202000482.

58 C. Wang, H. Lu, Z. Mao, C. Yan, G. Shen and X. Wang, Bimetal Schottky Heterojunction Boosting Energy-Saving Hydrogen Production from Alkaline Water *via* Urea Electrocatalysis, *Adv. Funct. Mater.*, 2020, **30**, 2000556, DOI: 10.1002/adfm.202000556.

59 B. You, X. Liu, N. Jiang and Y. Sun, A General Strategy for Decoupled Hydrogen Production from Water Splitting by Integrating Oxidative Biomass Valorization, *J. Am. Chem. Soc.*, 2016, **138**, 13639–13646, DOI: 10.1021/jacs.6b07127.

60 Q. Zhou, T.-T. Li, J. Qian, Y. Hu, F. Guo and Y.-Q. Zheng, Self-supported hierarchical CuO x @Co 3 O 4 heterostructures as efficient bifunctional electrocatalysts for water splitting, *J. Mater. Chem. A*, 2018, **6**, 14431–14439, DOI: 10.1039/C8TA03120G.

61 C. Han, X. Zhang, T. T. Li, Y. Hu and J. Qian, Carbon Nanotubes Grown on CuO Nanoparticle-Decorated Porous Carbon Microparticles for Water Oxidation, *ACS Appl. Nano Mater.*, 2021, **4**, 12119–12126, DOI: 10.1021/acsanm.1c02659.

62 A. S. Sabir, E. Pervaiz, R. Khosa and U. Sohail, An inclusive review and perspective on Cu-based materials for electrochemical water splitting, *RSC Adv.*, 2023, **13**, 4963–4993, DOI: 10.1039/d2ra07901a.

63 P. Kim, A. Anderko, A. Navrotsky and R. E. Riman, Trends in structure and thermodynamic properties of normal rare earth carbonates and rare earth hydroxycarbonates, *Minerals*, 2018, **8**, 106, DOI: 10.3390/min8030106.

64 Y. Deng, A. D. Handoko, Y. Du, S. Xi and B. S. Yeo, In Situ Raman Spectroscopy of Copper and Copper Oxide Surfaces during Electrochemical Oxygen Evolution Reaction: Identification of CuIII Oxides as Catalytically Active Species, *ACS Catal.*, 2016, **6**, 2473–2481, DOI: 10.1021/acscatal.6b00205.

65 C. H. F. Peden, J. W. Rogers, N. D. Shinn, K. B. Kidd and K. L. Tsang, Thermally grown Si3N4 thin films on Si(100): Surface and interfacial composition, *Phys. Rev. B*, 1993, **47**, 15622–15629, DOI: 10.1103/PhysRevB.47.15622.

66 G. Schön, High resolution Auger electron spectroscopy of metallic copper, *J. Electron Spectrosc. Relat. Phenom.*, 1972, **1**, 377–387, DOI: 10.1016/0368-2048(72)80039-2.

67 A. N. Mansour, Copper Mg K α XPS Spectra from the Physical Electronics Model 5400 Spectrometer, *Surf. Sci. Spectra*, 1994, **3**, 202–210, DOI: 10.1116/1.1247748.

68 M. Pelavin, D. N. Hendrickson, J. M. Hollander and W. L. Jolly, Phosphorus 2p electron binding energies. Correlation with extended Hückel charges, *J. Phys. Chem.*, 1970, **74**, 1116–1121, DOI: 10.1021/j100700a027.

69 R. Kaufmann, H. Klewe-Nebenius, H. Moers, G. Pfennig, H. Jenett and H. J. Ache, XPS studies of the thermal behaviour of passivated Zircaloy-4 surfaces, *Surf. Interface Anal.*, 1988, **11**, 502–509, DOI: 10.1002/sia.740111003.

70 T. P. Moffat, R. M. Latanision and R. R. Ruf, An X-ray photoelectron spectroscopy study of chromium-metalloid alloys-III, *Electrochim. Acta*, 1995, **40**, 1723–1734, DOI: 10.1016/0013-4686(95)00015-7.

71 B. Shokri, M. A. Firouzjah, S. I. Hosseini, FTIR analysis of silicon dioxide thin film deposited by metal organic-based PECVD, in *Proc. 19th Int. Plasma Chem. Soc.*, 2009, pp. 1–4, https://doi.org/www.ispc-conference.org.

72 M. H. Shahrokh Abadi, A. Delbari, Z. Fakoor and J. Baedi, Effects of annealing temperature on infrared spectra of SiO2 extracted from rice husk, *J. Ceram. Sci. Technol.*, 2015, **6**, 41–45, DOI: 10.4416/JCST2014-00028.

73 F. Adam and J. H. Chua, The adsorption of palmytic acid on rice husk ash chemically modified with Al(III) ion using the sol-gel technique, *J. Colloid Interface Sci.*, 2004, **280**, 55–61, DOI: 10.1016/j.jcis.2004.07.006.

74 X. Li, X. Hao, A. Abudula and G. Guan, Nanostructured catalysts for electrochemical water splitting: Current state and prospects, *J. Mater. Chem. A*, 2016, **4**, 11973–12000, DOI: 10.1039/c6ta02334g.

75 K. Asazawa, T. Sakamoto, S. Yamaguchi, K. Yamada, H. Fujikawa, H. Tanaka and K. Oguro, Study of Anode Catalysts and Fuel Concentration on Direct Hydrazine Alkaline Anion-Exchange Membrane Fuel Cells, *J. Electrochem. Soc.*, 2009, **156**, B509, DOI: 10.1149/1.3082129.

76 A. R. M. El-Gohary, A. Galal and N. F. Atta, Novel electrochemical sensor for simultaneous determination of amlodipine, atorvastatin, and acetylsalicylic acid based on carbon nanotubes-ferrocene/nickel chromium oxide nanocomposite, *Microchem. J.*, 2024, **200**, 110221, DOI: 10.1016/j.microc.2024.110221.

77 R. D. L. Smith, M. S. Prévot, R. D. Fagan, Z. Zhang, P. A. Sedach, M. K. J. Siu, S. Trudel and C. P. Berlinguette, Photochemical route for accessing amorphous metal oxide materials for water oxidation catalysis, *Science*, 2013, **340**, 60–63, DOI: 10.1126/science.1233638.

78 F. Song and X. Hu, Exfoliation of layered double hydroxides for enhanced oxygen evolution catalysis, *Nat. Commun.*, 2014, **5**, 4477, DOI: 10.1038/ncomms5477.

79 M. E. G. Lyons and R. L. Doyle, Oxygen evolution at oxidised iron electrodes: A tale of two slopes, *Int. J. Electrochem. Sci.*, 2012, **7**, 9488–9501, DOI: **10.1016/s1452-3981(23)16213-4**.

80 A. Grimaud, K. J. May, C. E. Carlton, Y. L. Lee, M. Risch, W. T. Hong, J. Zhou and Y. Shao-Horn, Double perovskites as a family of highly active catalysts for oxygen evolution in alkaline solution, *Nat. Commun.*, 2013, **4**, 2439, DOI: **10.1038/ncomms3439**.

81 O. A. Petrii and G. A. Tsirlina, Electrocatalytic activity prediction for hydrogen electrode reaction: intuition, art, science, *Electrochim. Acta*, 1994, **39**, 1739–1747, DOI: **10.1016/0013-4686(94)85159-X**.

82 B. E. Conway and G. Jerkiewicz, Relation of energies and coverages of underpotential and overpotential deposited H at Pt and other metals to the `volcano curve' for cathodic H2 evolution kinetics, *Electrochim. Acta*, 2000, **45**, 4075–4083, DOI: **10.1016/S0013-4686(00)00523-5**.

83 M. Faraday, VI. Experimental researches in electricity.-Seventh Series, *Philos. Trans. R. Soc. London*, 1834, **124**, 77–122, DOI: **10.1098/rstl.1834.0008**.

84 C. M. Gordon, J. D. Holbrey, A. R. Kennedy and K. R. Seddon, Ionic liquid crystals: Hexafluorophosphate salts, *J. Mater. Chem.*, 1998, **8**, 2627–2636, DOI: **10.1039/a806169f**.

85 R. A. Marcus and N. Sutin, Electron transfers in chemistry and biology, *Biochim. Biophys. Acta-Bioenerg.*, 1985, **811**, 265–322, DOI: **10.1016/0304-4173(85)90014-X**.

86 M. C. Henstridge, E. Laborda and R. G. Compton, Asymmetric Marcus-Hush model of electron transfer kinetics: Application to the voltammetry of surface-bound redox systems, *J. Electroanal. Chem.*, 2012, **674**, 90–96, DOI: **10.1016/j.jelechem.2012.04.006**.

87 A. J. Bard, L. R. Faulkner, Buttler-Volmer Model of Electrode Kinetics, in *Electrochem. Methods Fundam. Appl., Second*, John Wiley & Sons, Inc., New York, 2001, pp. 92–115, **https://www.wiley.com/en-us/Electrochemical+Methods:+Fundamentals+and+Applications,+2nd+Edition-p-9780471043720**.

88 D. Wang, W. Yan, S. H. Vijapur and G. G. Botte, Enhanced electrocatalytic oxidation of urea based on nickel hydroxide nanoribbons, *J. Power Sources*, 2012, **217**, 498–502, DOI: **10.1016/j.jpowsour.2012.06.029**.

89 J. O. M. Bockris, Kinetics of activation controlled consecutive electrochemical reactions: Anodic evolution of oxygen, *J. Chem. Phys.*, 1956, **24**, 817–827, DOI: **10.1063/1.1742616**.

90 B. E. Conway and B. V. Tilak, Behavior and Characterization of Kinetically Involved Chemisorbed Intermediates in Electrocatalysis of Gas Evolution Reactions, *Adv. Catal.*, 1992, **38**, 1–147, DOI: **10.1016/S0360-0564(08)60006-1**.

91 B. E. Conway and T. C. Liu, Examination of electrocatalysis in the anodic O 2 evolution reaction at Pt through evaluation of the adsorption behaviour of kinetically involved intermediate states, *Proc. Roy. Soc. Lond. Math. Phys. Sci.*, 1990, **429**, 375–397, DOI: **10.1098/rspa.1990.0065**.

92 J. Rossmeisl, Z. W. Qu, H. Zhu, G. J. Kroes and J. K. Nørskov, Electrolysis of water on oxide surfaces, *J. Electroanal. Chem.*, 2007, **607**, 83–89, DOI: **10.1016/j.jelechem.2006.11.008**.

93 S. Garcia-Segura, E. Mostafa and H. Baltruschat, Electrogeneration of inorganic chloramines on boron-doped diamond anodes during electrochemical oxidation of ammonium chloride, urea and synthetic urine matrix, *Water Res.*, 2019, **160**, 107–117, DOI: **10.1016/j.watres.2019.05.046**.

94 D. Grujicic and B. Pesic, Electrodeposition of copper: the nucleation mechanisms, *Electrochim. Acta*, 2002, **47**, 2901–2912, DOI: **10.1016/S0013-4686(02)00161-5**.

95 R. Guo, Y. Zhang, X. Zhang, H. Yang and T. Hu, Synthesis of Co0·52Cu0·48/Cu@S–C arrays for the enhanced performance of hydrazine-assisted hydrogen production, *Int. J. Hydrogen Energy*, 2024, **68**, 472–480, DOI: **10.1016/j.ijhydene.2024.04.180**.

96 D. Khalafallah, Y. Zhang and Q. Zhang, Maximizing urea-/hydrazine-assisted electrolytic hydrogen production by defective nickel copper selenide nanostructures, *FlatChem*, 2024, **43**, 100602, DOI: **10.1016/j.flatc.2023.100602**.

97 Z. Chen, L. Wang, H. Li, S. Zeng, R. Li, H. Chen, Y. Zheng, Q. Yao and K. Qu, Highly enhanced bifunctionality by trace Co doping into Ru matrix towards hydrazine oxidation-assisted energy-saving hydrogen production, *Fuel*, 2024, **360**, 130602, DOI: **10.1016/j.fuel.2023.130602**.

98 R. A. Senthil, S. Jung, A. Min, A. Kumar, C. J. Moon, M. Singh and M. Y. Choi, Revealing the Impact of Pulsed Laser-Produced Single-Pd Nanoparticles on a Bimetallic NiCo2O4 Electrocatalyst for Energy-Saving Hydrogen Production *via* Hybrid Water Electrolysis, *ACS Catal.*, 2024, **14**, 3320–3335, DOI: **10.1021/acscatal.3c05051**.

99 S. Behera, C. Chauhan and B. Mondal, Co–N–C/C Bifunctional Electrocatalyst for Dual Applications in Seawater Electrolysis and Catalyst in Hydrazine Fuel Cells, *Small*, 2024, 2311946, DOI: **10.1002/smll.202311946**.

100 U. P. Suryawanshi, U. V Ghorpade, P. V Kumar, J. S. Jang, M. He, H. J. Shim, H. R. Jung, M. P. Suryawanshi and J. H. Kim, Dopant induced hollow Ni2P nanocrystals regulate dehydrogenation kinetics for highly efficient solar-driven hydrazine assisted H2 production, *Appl. Catal., B*, 2024, **355**, 124165, DOI: **10.1016/j.apcatb.2024.124165**.

101 V. V Burungale, H. Bae, M. A. Gaikwad, P. Mane, J. Heo, C. Seong, S.-H. Kang, S.-W. Ryu and J.-S. Ha, Cu2O-based trifunctional catalyst for enhanced alkaline water splitting and hydrazine oxidation: Integrating sulfurization, Co incorporation, and LDH heterostructure, *Chem. Eng. J.*, 2024, **486**, 150175, DOI: **10.1016/j.cej.2024.150175**.

102 X. Liu, H. Mao, G. Liu, Q. Yu, S. Wu, B. Li, G. Zhou, Z. Li and L. Wang, Metal doping and Hetero-engineering of Cu-doped CoFe/Co embedded in N-doped carbon for improving trifunctional electrocatalytic activity in alkaline seawater, *Chem. Eng. J.*, 2023, **451**, 138699, DOI: **10.1016/j.cej.2022.138699**.

103 Y. Zhao, Y. Sun, H. Li, S. Zeng, R. Li, Q. Yao, H. Chen, Y. Zheng and K. Qu, Highly enhanced hydrazine oxidation on bifunctional Ni tailored by alloying for energy-efficient hydrogen production, *J. Colloid Interface Sci.*, 2023, **652**, 1848–1856, DOI: **10.1016/j.jcis.2023.09.003**.